RESEARCH ARTICLE

ADVANCED MATERIALS TECHNOLOGIES

www.advmattechnol.de

Smart Refreshable Braille Display Device Based on Magneto-Resistive Composite with Triple Shape Memory

Tao Hu, Shouhu Xuan, Yinduan Gao, Quan Shu, Zhenbang Xu, Shuaishuai Sun, Jun Li, and Xinglong Gong**

Braille devices made from stimuli-active polymers have provided a new approach for obtaining information on Braille text. However, it is still essential to find a more convenient and effective method to develop multifunctional Braille devices with shape memory effects to broaden their applications. Here, a novel smart refreshable Braille display based on triple-shape memory and magnetoresistive composite is developed with the advantages of simple fabrication, multifunctionality, and harmlessness for blind people. The triple shape memory effect enables this device to record the Braille text information and display the text using a complex Braille dot array. The stimuli-dependent conductivity produces a simultaneous electrical sensing signal when Braille dots are touched, thus the reading areas can be distinguished. Therefore, this multifunctional flexible composite has the potential to realize a refreshable and portable Braille e-book in the future.

1. Introduction

Visually challenged people are experiencing an impaired vision that prevents them from reading conventional books. Therefore, the Braille text was created, with each Braille letter consisting of six dots in three rows and two columns. Using Braille text, the visually challenged could obtain information by the feel of the pattern in the Braille books.[1–6] Recently, to replace traditional Braille books that were bulky and could not be refreshed once recorded, various types of refreshable Braille devices have been developed.[7–12] To achieve the real-time actuation of Braille dots, the integration of Braille dots and actuating parts is important for devices, such as a combination of a shape memory alloy (SMA) coil actuator and magnetic latch,[13] or electrolyte layer operated by a thin-film transistor,[8] compact dielectric elastomer tubular actuator,[14] passive and scalable magnetic mechanism for Braille cursor,[10] and dielectric film actuated by a triboelectric nanogenerator.[15] In particular, Braille devices made of electroactive polymers, such as dielectric elastomers, are flexible and stretchable, so they can provide a better tactile perception. However, the actuating performance of electroactive polymers relies heavily on the high-voltage supply, and these Braille devices may be potentially hazardous to the visually challenged. Thus, a safer, more convenient, and an effective approach for developing refreshable Braille display devices is in demand.

Shape memory polymers (SMPs) possess the advantages of flexibility and shape memory capability. These can be deformed and molded into a temporary shape, and then recovered at different temperatures, lighting conditions, and salt concentrations in solution.[16–26] The heat-triggered SMP possesses a shape memory effect similar to that of SMA. It can be programmed into a temporary shape when the temperature is higher than the melting point of the temperature-controlling component, then fixed through cooling, and finally reverted to its original shape through reheating. Therefore, Braille dots made from SMP can effectively meet the shape manipulation required for refreshable Braille devices. Traditional Braille devices can only offer readable and refreshable Braille texts. These can neither distinguish the exact Braille letters touched nor emphasize these Braille letters. Thus, in situ sensing is required in Braille devices to promote the interaction between humans and devices. Their restrictive functionality has confined the development of SMP-based Braille devices, so the integration of SMP and other responsive materials would be beneficial for developing reprogrammable and multifunctional SMP-based refreshable Braille devices with in situ sensing capability.

T. Hu, S. Xuan, Y. Gao, Q. Shu, X. Gong
CAS Key Laboratory of Mechanical Behavior and Design of Materials
Department of Modern Mechanics
CAS Center for Excellence in Complex System Mechanics
University of Science and Technology of China
Hefei 230027, P. R. China
E-mail: xuansh@ustc.edu.cn; gongxl@ustc.edu.cn

Z. Xu
CAS Key Laboratory of On-orbit Manufacturing and Integration for Space Optics System
Changchun Institute of Optics
Fine Mechanics and Physics
Chinese Academy of Sciences
Changchun, Jilin 130033, China

S. Sun
CAS Key Laboratory of Mechanical Behavior and Design of Materials
Department of Precision Machinery and Instrumentation
University of Science and Technology of China
Hefei, Anhui 230027, China

J. Li
Anhui Weiwei Rubber Parts Group Co. Ltd.
Tongcheng, Anhui 231400, China

The ORCID identification number(s) for the author(s) of this article can be found under https://doi.org/10.1002/admt.202100777.

DOI: 10.1002/admt.202100777

Owing to its high electrical and thermal conductivity, arbitrary shape reconfigurability, and self-healing capability, liquid metal (LM) has been widely employed in hybrid elastomers for flexible sensors, conductors, and soft robotics.[27–40] The LM breaks into microdroplets and is embedded in the polymer matrix. Numerous percolation pathways are formed by LM microdroplets through contact with their neighbors; thus, the LM embedded elastomers (LMEEs) change from insulating to conductive under compression. The LM also endows the LMEEs with shape-memory capability.[25,41–43] When the temperature is higher than the melting point of LM, the molten LM microdroplet deforms with the LMEEs, following which the LMEEs are fixed through cooling at a temperature lower than the freezing point of LM, and the shape is finally recovered through reheating. Thus, LMEEs with good electrical/thermal conductivity and shape memory capability can also be employed in smart Braille devices. However, LMEEs are often non-sensitive to stimuli because of the high surface tension of the LM microdroplets.[24] In LMEE-based Braille devices, the sensing capability is indispensable because these devices need to adjust the Braille texts based on the tactile sensing from the touched area. The single temporary shape further limits the development of LMEE-based Braille devices. Thus, Braille devices based on polymer composites consisting of LMEE with higher sensitivity, better response performance, and stable shape memory capability are immediately required.

Owing to the good mechanical properties of non-magnetic matrices and the unique magneto-induced capability of ferromagnetic particles, magnetorheological elastomers (MREs) have promising applications, such as untethered actuation,[26,44–49] vibration control,[50–53] and non-contact sensing.[31,36,54–58] Under an external magnetic field, the magnetic interactions of the particles actuate the matrix, and the gaps between the conductive fillers and magnetic particles are varied, resulting in changing conductivity. The introduction of ferromagnetic particles, such as iron and nickel, into LMEEs can significantly enhance the sensing performance of LMEEs.[26,28] These particles not only establish additional percolation pathways among LM droplets and improve the response performance, but also assemble along the external magnetic field and allow untethered actuation in the devices. Therefore, combining the shape memory effect of SMP, high electrical and thermal conductivity of LM, and good resilience and magnetic field-dependent property of MRE can be a new approach for developing a smart refreshable Braille display device (SRBDD) with stable deformation capability, good tactile perception, and multiple sensitivity.

In this study, a novel SRBDD based on a magnetoresistive composite with a triple-shape memory effect and magnetic field/compression dependent conductivity (PL-MRE) was developed. The PL-MRE was produced by melt-blending high-temperature liquid metal (HLM) and polycaprolactone (PCL) into a carbonyl iron particle (CIP)-doped polydimethylsiloxane (PDMS) matrix. In this multifunctional composite, the melting of PCL and HLM particles was selectively controlled by varying the temperature. Thus, the PL-MRE achieved a heat-triggered triple-shape memory effect with good repeatability, and a possible mechanism was proposed to analyze this temperature-dependent performance. Additionally, the gaps between the HLM particles and CIPs could be synchronously changed using different compressive strains and magnetic flux densities, leading to conductivity variations. When the Braille dots were touched, the touched areas could be clearly distinguished by the PL-MRE array. Finally, an SRBDD was constructed using a PL-MRE array and a polytetrafluoroethylene (PTFE) mold, with good display performance and a potential in smart refreshable Braille e-books.

2. Results and Discussion

2.1. Design of PL-MRE

The fabrication process of the PL-MRE is schematically illustrated in **Figure 1**a. The PL-MRE possessed good flexibility and stretchability owing to the stable mechanical properties of the PDMS matrix (Figure 1b–d). This soft composite could be easily bent and twisted without any damage. The PL-MRE array can also tolerate finger pressing and retain the shape of Braille dots. Owing to the unique phase change properties of PCL and HLM, PDMS-PCL-LM and PL-MRE exhibited triple-shape memory effects. Differential scanning calorimetry (DSC) curves clearly showed the phase change processes of PCL and HLM (Figure 1e–g). The PDMS-PCL showed one endothermic peak, while PDMS-PCL-LM and PL-MRE exhibited two endothermic peaks during the heating process, showing that both PCL crystals and HLM particles were melted. Here, the melting point of PCL varied 54.4, 58.9, and 59.4 °C in PDMS-PCL, PDMS-PCL-LM, and PL-MRE. That of HLM varied as 53.1, and 50.8 °C in PDMS-PCL-LM and PL-MRE. Slight shifts were observed in the endothermic peaks of these samples, indicating that the PDMS/PCL/HLM blend system was immiscible.[59] The compatibility among the PCL crystals, HLM particles, and PDMS matrix was poor at room temperature. Thus, the PCL crystals and HLM particles could be pulled out from the PDMS matrix, and pits were formed on the incision interface while cutting the samples.

As shown in Figure 1h, the protrusions on the incision interface further indicated the removal of the PCL crystals. No ellipsoidal particle was found in PDMS-PCL, demonstrating that all the PCL pellets were melted and blended into the PDMS matrix with no residual components. For PDMS-PCL-LM, the irregular white particles embedded in the PDMS matrix indicated that HLM was broken into microparticles and homogenously separated (Figure 1i). The pits also proved the low compatibility between the HLM particles and the PDMS matrix. As shown in Figure 1j, numerous chain structures were formed by the CIPs inside the PL-MRE, while the HLM particles were embedded among CIP chains. The energy dispersive X-ray spectroscopy (EDS) elemental maps revealed the distribution of the CIPs and HLM particles more clearly (Figure 1k). The Fe element was only contained in the CIPs, so the chain-like distribution showed the magnetically induced assemblies of CIPs in the composites. The other metallic elements, such as Bi, Pb, In, and Sn, exhibited the same distribution, which proved that the HLM was uniformly dispersed in the PDMS matrix with a stable composition. No HLM-Fe alloy was found in PL-MRE, indicating that the CIPs were also immiscible with HLM. Thus, a PL-MRE composite with PCL crystals, HLM particles, and

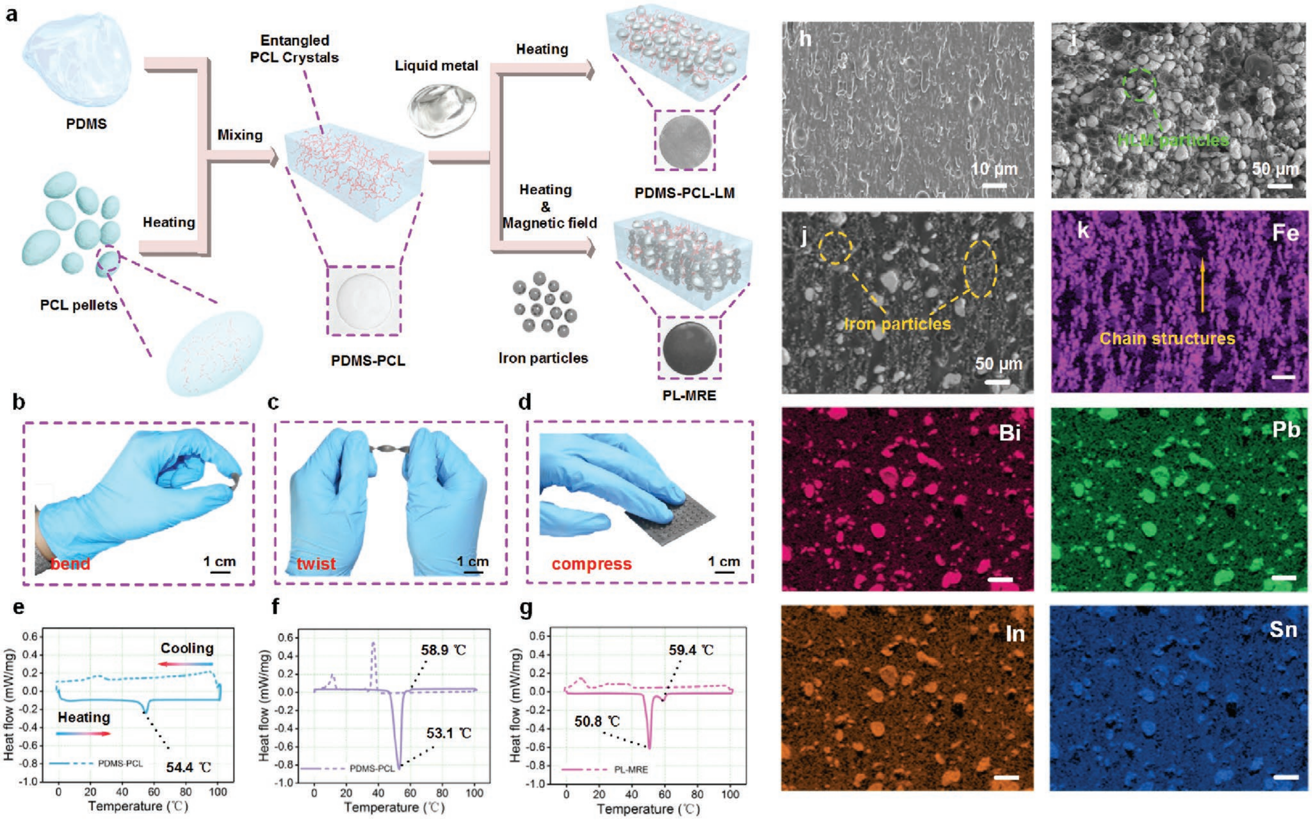

Figure 1. a) Fabrication processes of PL-MRE, digital images of PL-MRE under b) bending, c) twisting, and d) compressing. DSC curves of e) PDMS-PCL, f) PDMS-PCL-LM, and g) PL-MRE. SEM images of h) PDMS-PCL, i) PDMS-PCL-LM, and j) PL-MRE. k) EDS elemental mappings of PL-MRE.

CIPs was developed, which showed a new approach for multifunctional candidates for actuators and sensors.

2.2. Rheological Properties

The mechanical properties of PL-MRE determined the tactile sensation and deformation capability of Braille dots, while the component ratio significantly affected the flexibility and strength of PL-MRE. The phase change properties of PCL and HLM endowed PL-MRE with temperature-dependent mechanical properties; thus, the influence of the component ratio and temperature on the shear rheological performance of PL-MRE was systematically investigated. All the samples in the rheological tests were 20 mm in diameter and 1 mm in thickness. The shear strain oscillated at a constant frequency of 5 Hz with amplitude of 0.1%. First, the PDMS-PCL samples with a curing ratio of 1:10 and different PCL weight fractions (10–70 wt%) were tested. As the temperature T increased from 15 to 80 °C, the shear storage modulus G' of PDMS-PCL significantly decreased (**Figure 2**a). For 20 wt% PDMS-PCL, G' ranged from 185 to 52 kPa, while it varied from 473 to 15 kPa for 70 wt% PDMS-PCL. When T was higher than 55 °C, a rapid decrease in G' occurred in all PDMS-PCL samples and the loss factor suddenly increased (Figure 2b,c). These results indicate that the PCL crystals melted, which agreed with the DSC results shown in Figure 1e. As the ratio of PCL pellets increased, more PCL crystals were found in the PDMS matrix at 15 °C, so the initial modulus G_0' of PDMS-PCL increased. However, the PCL crystals melted into amorphous PCL chains when T was higher than 55 °C, which resulted in the severe weakening of PDMS-PCL. Moreover, as the curing ratio of PDMS decreased to 1:20 and 1:25, the corresponding G' also weakened (Figure 2d–f). After changing the PDMS matrix with the Ecoflex 00 30 matrix, the sample further softened and continued exhibiting a rapid decrease at 55 °C. Thus, owing to the stable phase change property of PCL, it could be employed as a temperature-controlling component in these SMP composites.

After adding HLM to the PDMS-PCL precursor, the color of the mixture changed from white to gray, and the content of HLM critically influenced the mechanical properties of the PDMS-PCL-LM. Here, the volume fraction of HLM was used to represent its content due to the high density (9.36 g cm^{-3}). The shear creep test of the PDMS-PCL-LM was conducted to further evaluate its thermal stability and resilience (**Figure 3**a–c). The shear strain gradually increased with T under 1 kPa shear stress, indicating the softening characteristics of the samples. When T was above 45 °C, the shear strain surged, indicating the melting of the HLM particles. After the shear stress was unloaded, the shear strain synchronously dropped, indicating the good resilience of the PDMS matrix. By increasing the shear stress from 1 to 2 and 3 kPa, the shear strain was enhanced, which further proved the stable mechanical properties of the PDMS-PCL-LM.

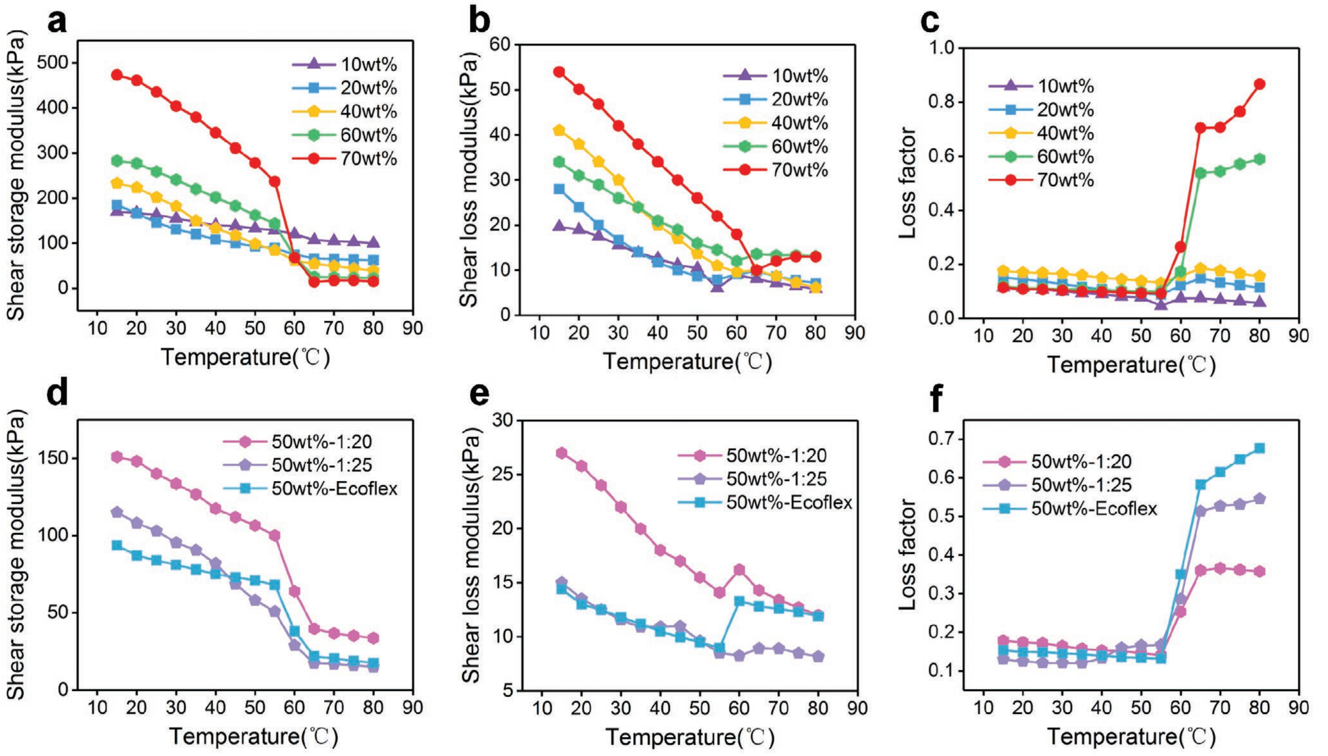

Figure 2. Temperature-dependent a) shear storage modulus, b) loss modulus, and c) loss factor of PDMS-PCL with PCL weight fraction from 10 to 70 wt%, the temperature-dependent d) shear storage modulus, e) loss modulus, and f) loss factor of PDMS-PCL with different curing ratio.

The melting point of HLM was lower than that of PCL, so the HLM particles melted earlier than PCL crystals during the heating process. When the volume fraction of HLM was maintained at 30 vol%, the PDMS-PCL-LM exhibited two rapid decreases in G' at 45 and 55 °C (Figure 3d–f). Thus, the first decrease $\Delta G_1'$ was caused by the melting of HLM particles and the second decrease $\Delta G_2'$ by the melting of PCL crystals. For the 50 vol% HLM samples, $\Delta G_1'$ significantly increased, and $\Delta G_1'$ was much larger than $\Delta G_2'$ because the content of HLM was much higher than that of PCL in this sample (Figure 3g–i). Therefore, HLM could be used as another temperature-controlling component owing to its stable phase change property. However, the 50 wt% PCL–50 vol% HLM precursor could not be successfully cured because too many PCL crystals and HLM particles break the cross-linking networks of the PDMS matrix. Therefore, the synergistic effect of PCL and HLM on the temperature-dependent mechanical properties should be considered.

Tensile failure tests were conducted on dumbbell-shaped samples to further evaluate the mechanical properties of the composites. As the PCL content increased from 0 to 60 wt%, the tensile failure strain evidently weakened (**Figure** 4a), because excessive PCL crystals made the sample stiff and brittle. To retain both the temperature-dependent property and stretchability of PDMS-PCL, 20 wt% was chosen as the ideal weight fraction of PCL. Adding HLM to the PDMS-PCL precursor at concentrations ranging from 10 to 65 vol% resulted in varying enhancement of the tensile failure strain, demonstrating the formation of porous structures with good stability (Figure 4b). However, excess HLM particles led to numerous pits in the PDMS matrix (Figure 1i). The cross-linking networks formed by the PDMS molecular chains were broken and the PDMS-PCL-LM was greatly weakened. Here, 20–40 vol% was the ideal range of HLM particle volume fraction in PDMS-PCL-LM owing to its appropriate strength and stretchability.

Subsequently, the CIPs and HLM were mixed into a 20 wt% PDMS-PCL precursor to fabricate PL-MRE. Here, the volume fraction of the CIPs and HLM was maintained at 28 vol%. After increasing the CIP volume fraction, the PL-MRE became stiffer, and the tensile failure strain was dramatically weakened (Figure 4c). The CIPs endowed the PL-MRE with unique magneto-induced properties; therefore, samples with different CIP contents were first tested with HyMDC to evaluate the magnetization properties. As the CIP content increased from 7 to 28 vol%, the saturation magnetization of PL-MRE increased from 35.2 to 150.1 emu g^{-1} (Figure 4d), revealing the stable magnetization property of CIPs in this blend system. At 15 °C, the G_0' of PL-MRE increased from 0.14 to 0.89 MPa with CIP, showing the enhancement of CIPs (Figure 4e,f). When T reached 80 °C, the PL-MRE exhibited a typical magneto-induced property under a 900 mT magnetic field (Figure 4g–i). By increasing the CIP content, more CIP chains were formed during the pre-structuring process. Thus, the magnetic interactions among the chains dramatically increased, which caused a stronger magneto-induced effect. A low CIP volume fraction resulted in a weak response of PL-MRE to the magnetic field, while excess CIP greatly weakened the stretchability and flexibility of PL-MRE. Therefore, 21 vol% was selected as the desired volume fraction of CIPs owing to its suitable strength and magnetization properties. Thus, the stable magneto-response

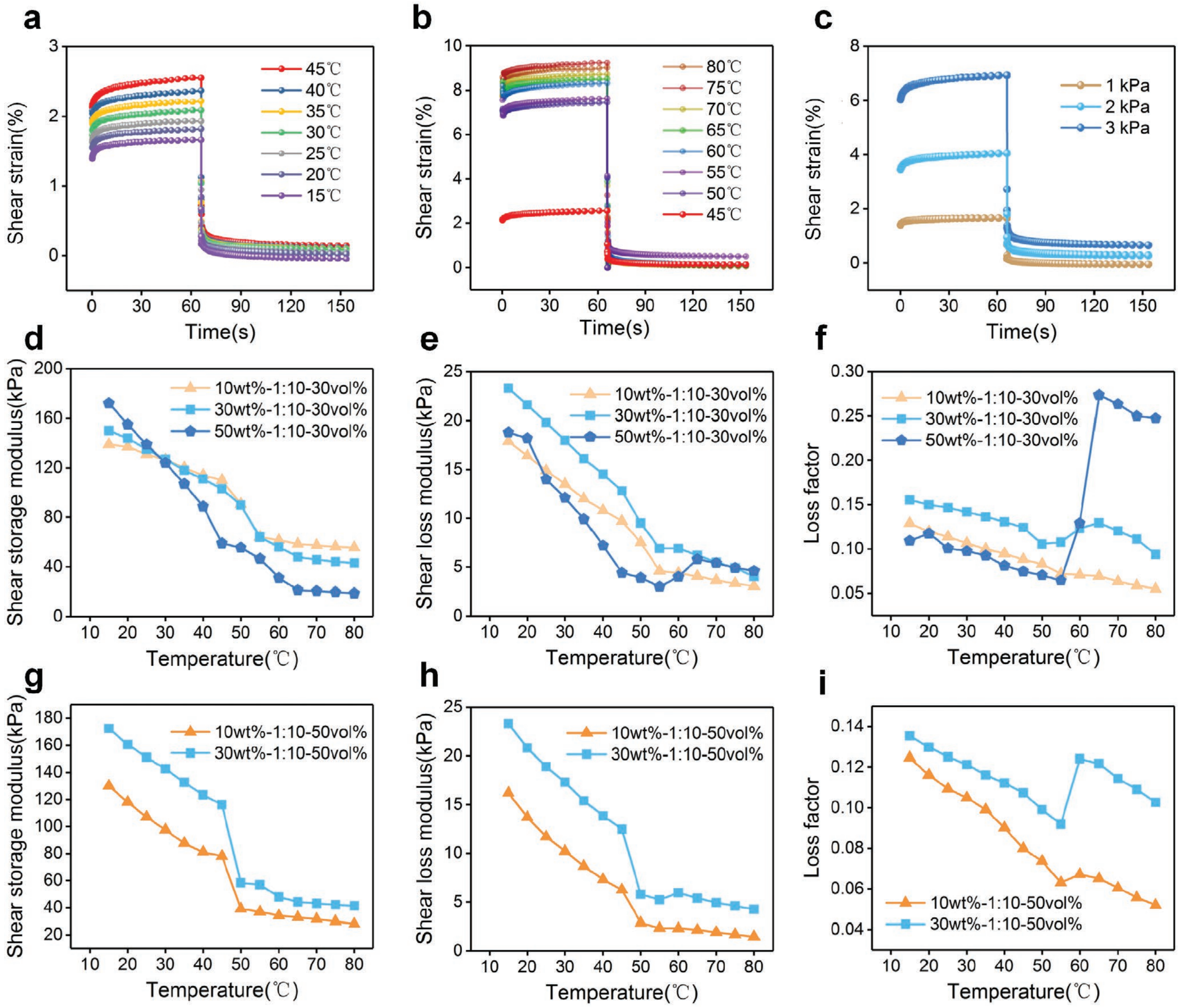

Figure 3. Shear creep tests of PDMS-PCL-LM at different temperature and shear stress: a) 15 to 45 °C, b) 45 to 80 °C, and c) 1 to 3 kPa, the temperature-dependent d) shear storage modulus, e) loss modulus, and f) loss factor of PDMS-PCL-LM with HLM volume fraction of 30 vol%, the temperature-dependent g) shear storage modulus, h) loss modulus, and i) loss factor of PDMS-PCL-LM with HLM volume fraction of 50 vol%.

properties of CIPs and good phase change properties of PCL and HLM guaranteed that PL-MRE could be employed in multifunctional composites with good temperature and magnetic field response performance.

2.3. Compression Response Performance

The introduction of HLM and CIPs significantly enhanced the conductivity of the PL-MRE. The PL-MRE composite with good flexibility, mechanical strength, and magneto-induced properties is potentially useful for applications in multifunctional sensing devices. Therefore, the compression response performance of the PL-MRE sensor at room temperature (25 °C) was studied. During the compression test, a 3D-printed cylinder (20 mm in diameter) was fixed on the DMA clamps to compress the PL-MRE sensor (20 mm in diameter and 1 mm in thickness) on the compression platform (**Figure 5**a). The mechanical and electrical signals were recorded using a DMA and a Modulab material test system, respectively.

First, we explored the piezo-conductivity of PDMS-PCL-LM without the addition of any CIPs. Owing to the high electrical conductivity of HLM, the introduction of HLM made the insulating PDMS-PCL conductive, and its resistance R dropped sharply with increasing HLM content (Figure 5b). Specifically, it decreased from 7.9 to 1 MΩ and 58 Ω when the HLM volume fractions increased from 51 to 53 and 54 vol%, respectively. Once the HLM volume fraction was above 53 vol%, stable percolation networks were established by HLM particles; thus, an increase of several orders of magnitude could be found in conductivity σ. The σ and compressive force F_c of 53 vol% PDMS-PCL-LM quickly reached 2.61 μS m^{-1} and 11.96 N under 5% compressive

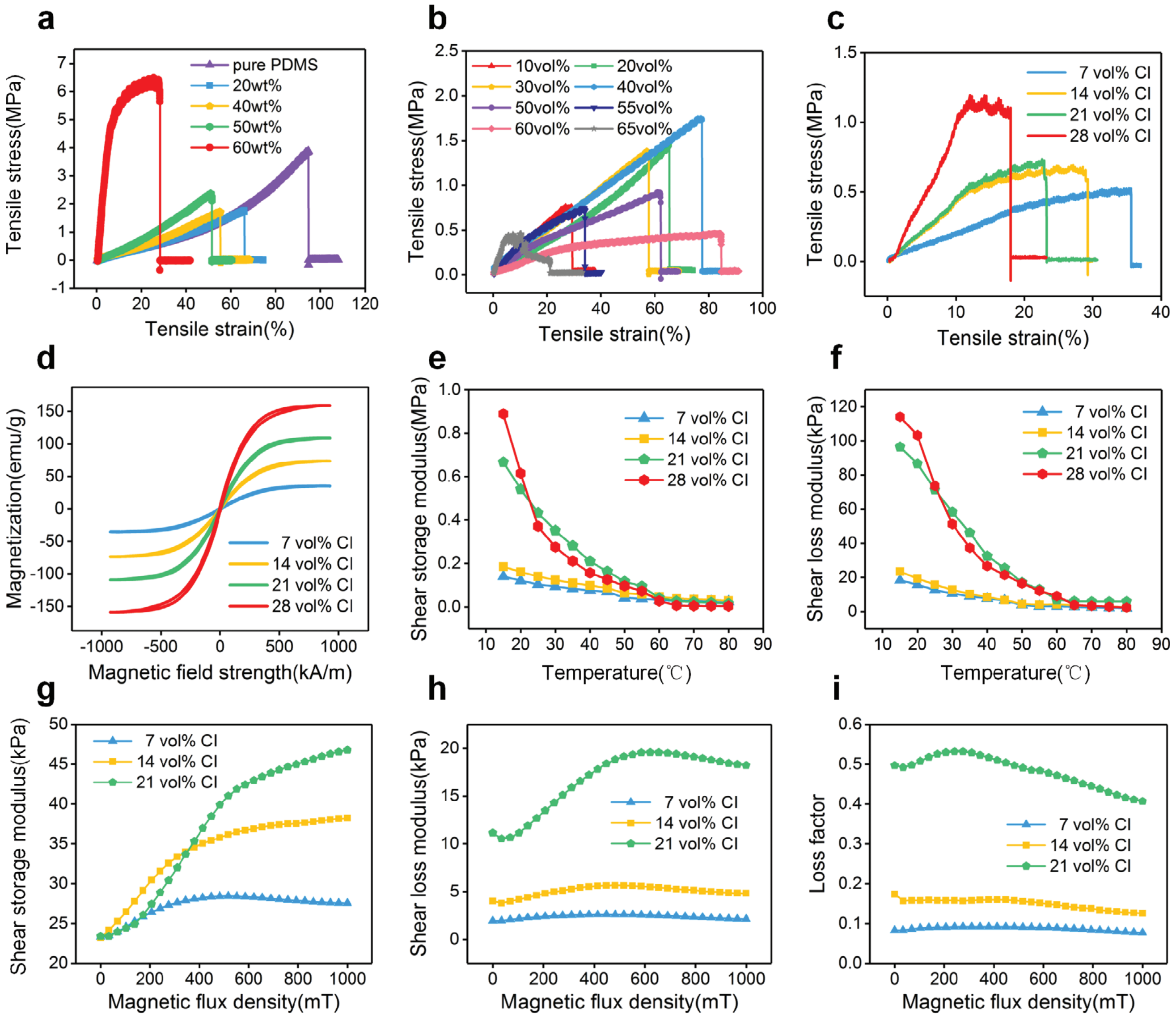

Figure 4. The tensile stress–strain curve of a) PDMS-PCL, b) PDMS-PCL-LM, and c) PL-MRE, d) the magnetization curves of PL-MRE with CIP volume fraction from 7 to 28 vol%, the temperature-dependent e) shear storage modulus and f) loss modulus of PL-MRE, g) shear storage modulus, h) loss modulus, and i) loss factor of PL-MRE versus magnetic flux density.

strain with good repeatability (Figure 5c). Here, the volume fraction of HLM and CIP in the PL-MRE samples was set at 28 vol% to avoid the PL-MRE from becoming completely conductive with a weak response to stimuli or too stiff with low flexibility.

Subsequently, the 21 vol% CI sample was chosen for the cyclic compression tests. At a compressive frequency of 0.1 Hz, both σ and F_c of the PL-MRE sensor synchronously varied with compressive strain (Figure 5d,e). The $\Delta\sigma$ and ΔF_c reached as high as 663.2% and 48.0 N under 9% compressive strain, respectively. Owing to the Mullis effect, the electrical and mechanical responses of the PL-MRE sensor were weakened, but they could return to their original state in the low compressive strain range, showing good repeatability. Here, the piezo-conductivity coefficient PCC ($\frac{\Delta\sigma/\sigma_0}{\varepsilon_c}$, where ε_c is the compressive strain) was used to evaluate the compression response performance of the PL-MRE sensor. It was 27 and 135.9 in the yellow (ε_c from 1 to 5%) and blue (ε_c from 5 to 9%) regions, respectively (Figure 5f). In the yellow region, the PL-MRE sensor was slightly compressed, the gaps and pits among the CIPs, HLM particles, and PDMS matrix slightly changed, and $\Delta\sigma/\sigma_0$ gradually increased. Once the PL-MRE sensor was completely squeezed, the particles were fully embedded in the PDMS matrix. In this case, considerably more contact between the conductive particles was formed for the deformation of the PDMS matrix; thus, the electrical responses of the PL-MRE sensor rapidly increased.

Moreover, both $\Delta\sigma/\sigma_0$ and F_c changed linearly with ε_c under triangular compression. The PL-MRE sensor exhibited very low hysteresis in the loading and unloading phases, proving the feasibility of the multifunctional strain sensor (Figure 5g). The compression responses of the PL-MRE were also barely affected

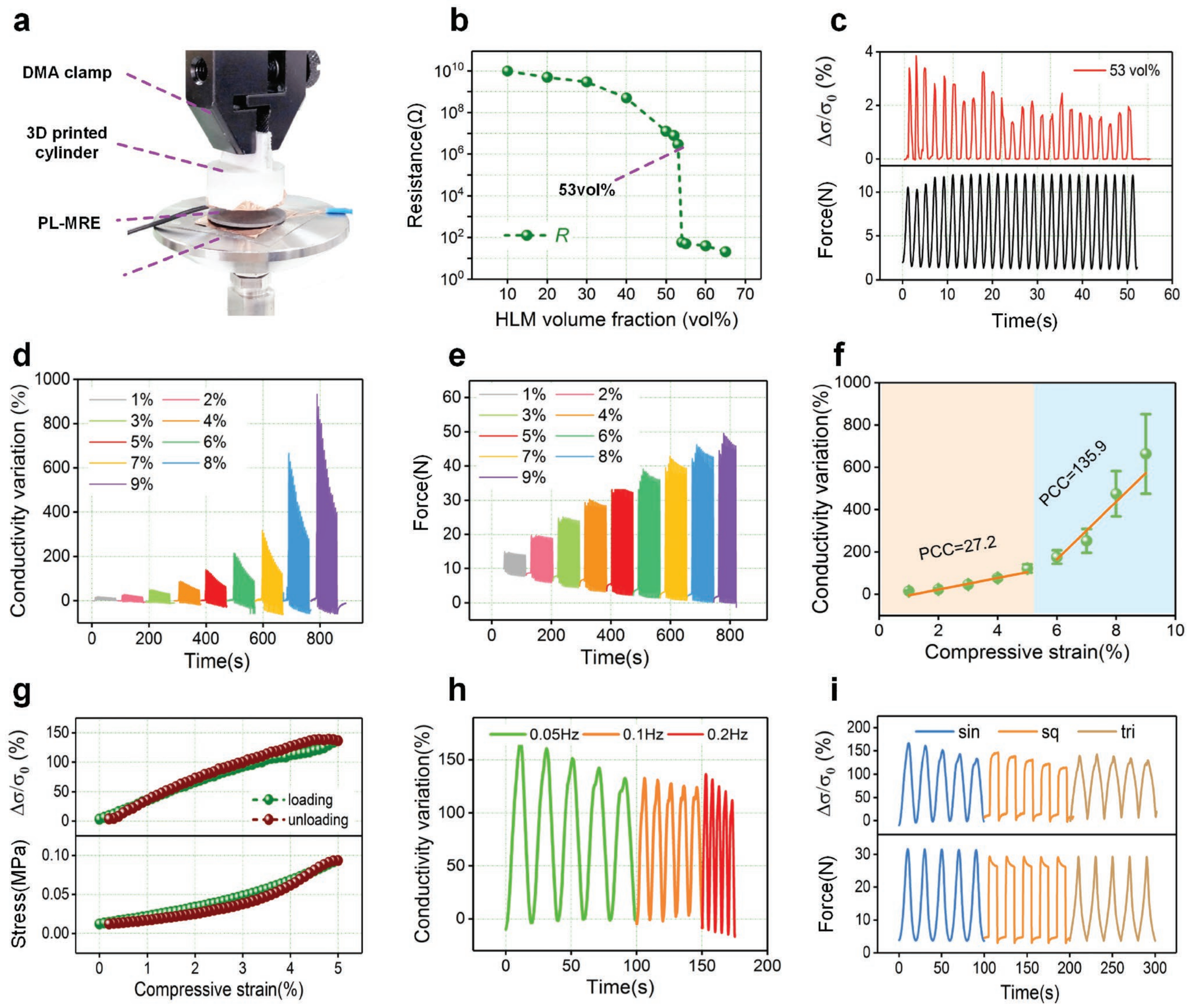

Figure 5. a) The compression testing system: DMA clamp, 3D-printed cylinder, PL-MRE sample, and compression platform. The compression test results: b) the resistance of PDMS-PCL-LM sensor versus HLM volume fraction, c) electrical and mechanical responses of PDMS-PCL-LM under cyclic compression, compressive strain dependent d) $\Delta\sigma/\sigma_0$ and e) force of PL-MRE, f) $\Delta\sigma/\sigma_0$ versus compressive strain amplitude, g) the hysteresis of electrical and mechanical responses in loading and unloading phases of triangle compression, h) the $\Delta\sigma/\sigma_0$ versus compressive frequency under the amplitude of 5%, i) the electrical and mechanical responses of PL-MRE under different loading waveforms.

by the loading frequency (Figure 5h). After increasing frequency from 0.05 to 0.1 and 0.2 Hz, $\Delta\sigma/\sigma_0$ only varied from 142 to 130% and 137%, respectively. Finally, different loading waveforms, such as sine, square, and triangle, could be clearly distinguished by the PL-MRE (Figure 5i). The variation tendency of both $\Delta\sigma/\sigma_0$ and ΔF_c coincided with ε_c, and they recovered in each compress-release cycle. The good compression response performance further demonstrated the promise of the PL-MRE multifunctional composite in strain sensors.

2.4. Magnetic Field Response Performance

Owing to the stable magnetization property of CIP and the effective elasticity of the PDMS matrix, the conductivity of PL-MRE could also be synchronously varied by adjusting the applied magnetic field. Thus, the magnetic field response performance of PL-MRE was systematically investigated. PL-MRE was sandwiched between two copper foils, which were taped on the plate rotor and electromagnetic base of an MCR 302 rheometer (**Figure 6**a). The copper foil and Modulab material test system were connected by wires for conduction of electrical signals.

At room temperature (25 °C), the initial resistance R_0 of PL-MRE changed from 3160 MΩ to 18 kΩ, by increasing the CIP content from 0 (PCL-PDMS-LM) to 28 vol% (PCL-PDMS-CI) (Figure 6b). Its conductivity sharply increased with the increase in CIP content because more percolation pathways were formed by the CIPs. However, excess CIPs filled the PDMS matrix with particles, weakening the flexibility and magnetic

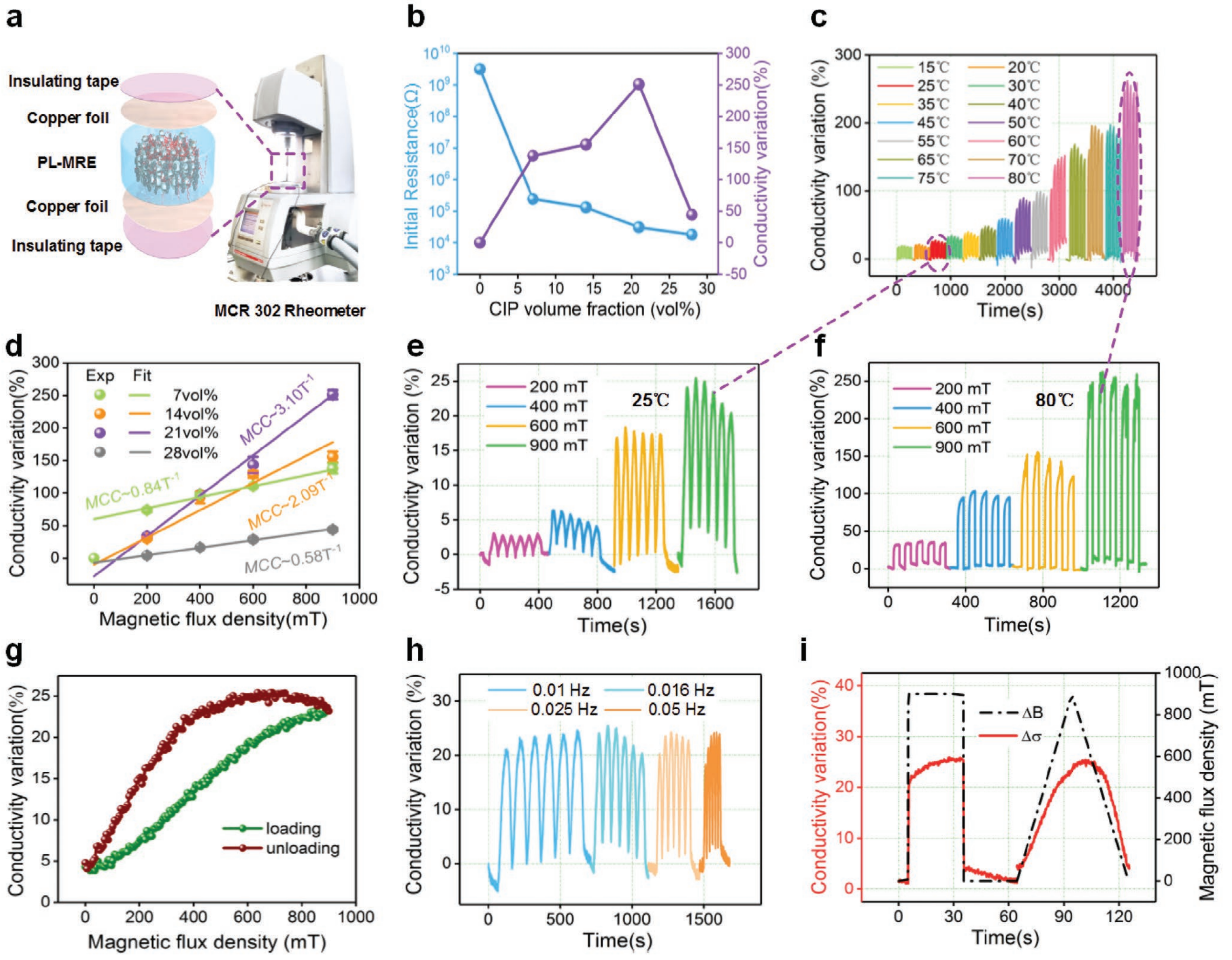

Figure 6. a) Schematic illustration of the magnetic-thermal testing system, b) the resistance and conductivity variation ($\Delta\sigma/\sigma_0$) of PL-MRE versus CIP volume fraction. The magnetic field response tests: c) magnetic field dependent $\Delta\sigma/\sigma_0$ of PL-MRE at different temperature, d) $\Delta\sigma/\sigma_0$ of PL-MRE with different CIP content versus magnetic flux density, typical $\Delta\sigma/\sigma_0$ under different magnetic flux density at e) 25 °C and f) 80 °C, g) the hysteresis of PL-MRE under a triangle waveform magnetic field at 25 °C, h) $\Delta\sigma/\sigma_0$ at different frequency under the amplitude of 900 mT, i) the comparison of responses under a triangle and square waveform magnetic field.

field response performance of PL-MRE. The relative conductivity variation was calculated using $\frac{\Delta\sigma}{\sigma_0}$, where σ_0 and $\Delta\sigma$ were the initial values and variations in conductivity, respectively. The $\Delta\sigma/\sigma_0$ under 900 mT magnetic field first increased with CIP content until it reached 21 vol%, which agreed with the above discussion. Therefore, 21 vol% was chosen as the ideal CIP volume fraction for cyclic magnetic sensing tests. Owing to the phase change properties of the HLM particles and PCL crystals, the magnetic response performance of PL-MRE was also influenced by T. As T changed from 15 to 80 °C, the $\Delta\sigma/\sigma_0$ dramatically increased from 20.3 to 254.1% at 900 mT (Figure 6c). In particular, the $\Delta\sigma/\sigma_0$ at both 25 and 80 °C exhibited good stability (Figure 6e,f). The melting of PCL crystals and HLM particles softened the PL-MRE, so that the binding force of the matrix to CIPs was reduced and the movement of CIPs gradually increased. More HLM particles and CIPs would favored contact with their neighbors during the movement of CIPs, and more percolating pathways were formed, leading to larger $\Delta\sigma/\sigma_0$.

Furthermore, the magneto-conductivity coefficient MCC was used to represent the magnetic–electrical coupling property of PL-MRE, which was calculated using $\frac{\Delta\sigma/\sigma_0}{\Delta B}$, where ΔB is the variation of magnetic flux density. The MCC of 21 vol% PL-MRE reached $3.10 \pm 0.07\ \mathrm{T}^{-1}$ with a fit coefficient of 0.9976 (Figure 6d), proving its feasibility as a multifunctional composite. Owing to the good elasticity of the PDMS matrix, a slight hysteresis was observed in the response of PL-MRE during the loading and unloading phases of a triangular magnetic field (Figure 6g). The effect of frequency on conductivity was then investigated (Figure 6h). After applying a 900 mT magnetic field, $\Delta\sigma/\sigma_0$ changed to 23.5%, 23.1%, 23.2%, and 23.7% at 0.01, 0.016, 0.025, and 0.05 Hz, respectively, which indicated that frequency hardly affected the performance of PL-MRE. Finally, a square and triangle magnetic field was applied to the

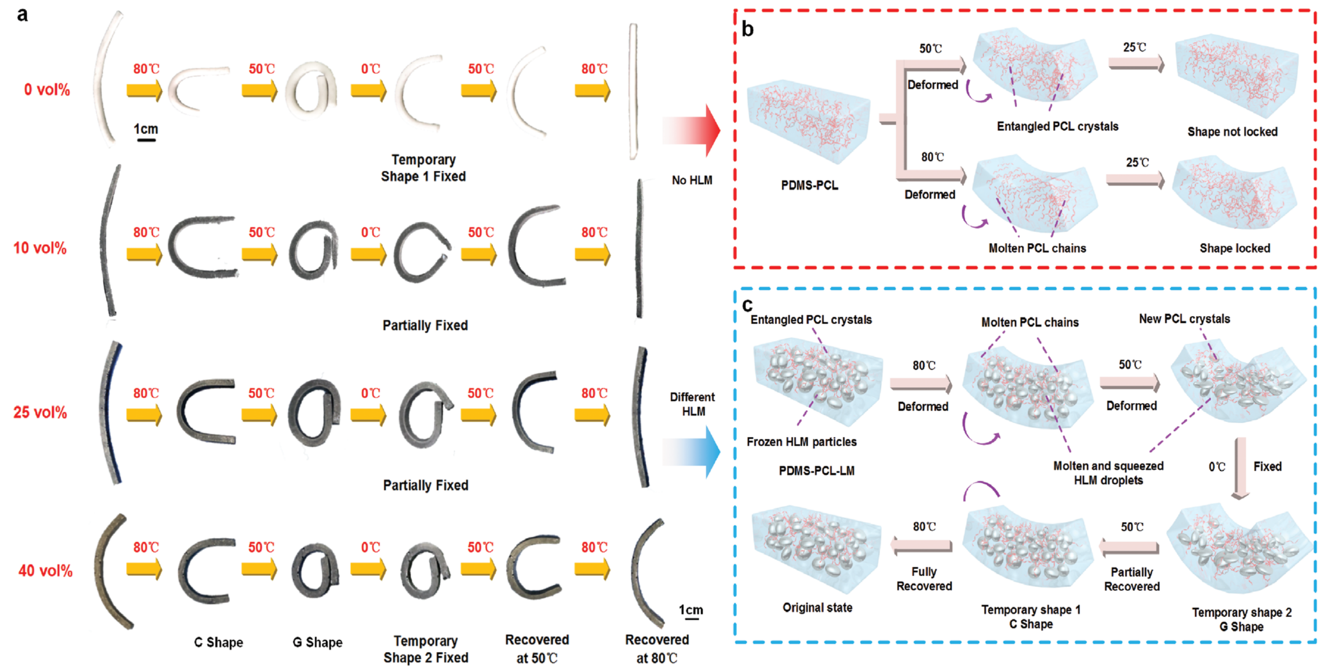

Figure 7. a) Digital images and b,c) schematic illustration for the shape memory process of PCL-PDMS and PCL-PDMS-LM.

PL-MRE, and it could easily distinguish the loading waveform (Figure 6i). The $\Delta\sigma/\sigma_0$ coincided with the magnetic flux density, further demonstrating the potential of PL-MRE in multifunctional composite sensors.

2.5. Shape Memory Property

The unique phase change characteristics of the PCL crystals and HLM particles changed the mechanical properties of the PL-MRE, endowing the PL-MRE with a triple-shape memory effect, which made it self-adaptable for detecting objects with complex morphologies. The PL-MRE possesses two reprogrammable temporary shapes owing to the different melting points of the temperature-controlling components (T_{pcl}= 58 °C, T_{hlm}= 47 °C). Herein, rod-shaped samples with dimensions of 60 mm × 3 mm × 3 mm were fabricated to evaluate the shape memory effect. First, the rod was heated at 80 °C for 5 min, then bent into a “C” shape (temporary shape 1) and fixed. It was then cooled at 50 °C for 5 min and further bent into a “G” shape (temporary shape 2). Subsequently, it was cooled at 0 °C for 5 min to lock all the shape transformations. The rods showed different shape memory effects when they were subjected to room temperature (25 °C) again. As shown in **Figure 7**a, by maintaining the PCL weight fraction at 20 wt%, the PDMS-PCL (0 vol% HLM) recovered into a “C” shape while the PDMS-PCL-LM (10–40 vol% HLM) partially recovered into an incomplete “G” shape. When the volume fraction of the HLM was above 40 vol%, the “G” shape was completely locked. By heating the rods at 50 °C again, all the rods deformed into a thinner “C” shape. After heating at 80 °C, the shape of the rods fully recovered to the original state, showing a triple shape memory effect.

A schematic illustration of the shape-memory effect is shown in Figure 7b,c. At 80 °C, all the entangled PCL crystals in PDMS-PCL melted into amorphous PCL chains and moved within the deformed rod (“C” shape). The molten PCL chains then crystallized at 50 °C with new entangled structures. During the deformation process to the “G” shape, the newly entangled PCL crystals and PDMS matrix stored the elastic energy. After cooling the rod to 25 °C again, they initiated shape recovery, preventing the rod from holding the “G” shape and allowing recovery into the “C” shape. When T increased again to 80 °C, the newly entangled PCL crystals melted again, and the energy stored in the PDMS matrix was released, driving the rod into its original shape. After adding the HLM particles, the molten HLM droplets moved within the rod at 50 °C (“G” shape), while the PCL crystals would still hold the “C” shape. After fixing at 0 °C and freezing at 25 °C, the newly frozen HLM particles could not tolerate the driving force of the PCL crystals and PDMS matrix, so the rod partially recovered into an incomplete “G” shape. When the HLM volume fraction was above 40 vol%, the frozen HLM particles was stiff enough to maintain the “G” shape, and the rod could be completely fixed into the “G” shape at 25 °C. Once reheated at 50 °C, the melting of HLM particles resulted in recovery to the “C” shape under the driving force of the PCL crystals and PDMS matrix. Upon further heating at 80 °C, both the HLM particles and PCL crystals melted, and the high resilience of the PDMS matrix prompted the rod to quickly return to its original shape.

2.6. SRBDD Based on PL-MRE

The above results show that PL-MRE possesses a good triple-shape memory effect and magnetic field/compression response

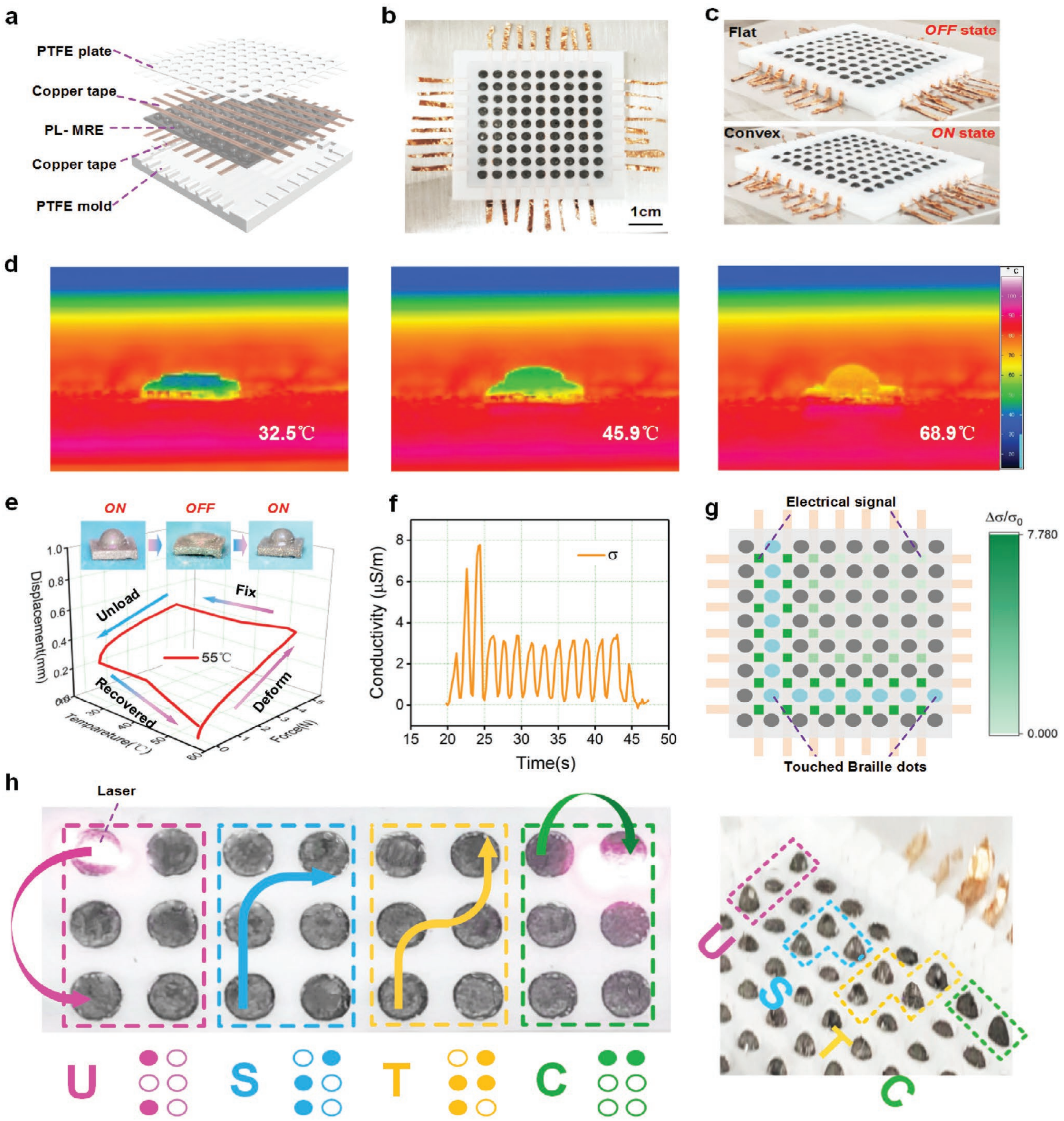

Figure 8. a) Schematic illustration and b) digital images of SRBDD-PL-MRE, c) digital images of SRBDD-PL-MRE in off and on state, d,e) thermal images, digital images, and a representative 3D plot for presenting shape memory property of a single Braille dot, f) electrical signals of SRBDD-PL-MRE under cyclic pressing, g) the 2D intensity profile of $\Delta\sigma/\sigma_0$ when touching the Braille dots on the boundary, h) Braille letters of "U", "S", "T", and "C" displayed by the SRBDD-PL-MRE.

performance. To prove the feasibility of PL-MRE in practical applications, a SRBDD based on PL-MRE (SRBDD-PL-MRE) was designed. The schematic illustration and digital images of the device are shown in **Figure 8**a–c. The SRBDD-PL-MRE consists of a PL-MRE array, copper tapes, and PTFE molds. The dimensions of the PL-MRE sensor array were 50 mm × 50 mm × 1 mm, with a 9 × 9 Braille dot structure (3 mm in diameter and 5 mm in distance) distributed on it. Copper tapes were adhered on the substrate between two columns of Braille dots, and finally the PL-MRE array was encapsulated in PTFE molds. A heating platform and near-IR (NIR) laser were employed to trigger the device.

By heating the SRBDD-PL-MRE to 80 °C on a heating platform for 5 min, all the PCL crystals and HLM particles were melted. A 3D-printed plate was then used to compress the Braille dots on the surface for 5 min. At this moment, the molten PCL chains and HLM droplets crystallized again; thus, the Braille dots were hidden in the porous PTFE plate. The surface of the SRBDD-PL-MRE became flat with negligible tactile sensation owing to the shape memory property of PL-MRE, which was marked as the "OFF" state (Figure 8c). After reheating at 80 °C, the Braille dots recovered to a convex shape again owing to the melting of the PCL crystals and HLM particles. The surface became touchable again, which was marked as the "ON" state. By heating different Braille dots on the surface, Braille letters with convex and flat Braille dot structures could be shown, so that the displayed Braille texts could be refreshed with good repeatability.

To further evaluate the properties of SRBDD-PL-MRE, thermal images of a single Braille dot were obtained (Figure 8d, Movie S2, Supporting Information). The T of the compressed Braille dot was quickly heightened by the heating platform. In 11 s, the T increased from 32.5 to 68.9 °C and the shape of Braille dot fully recovered. The Braille dot was then rapidly cooled in 5 s by placing it on a metal plate. Thus, the next Braille character could be displayed after 16 s. Moreover, the compression creep test of a single Braille dot was conducted using a rheometer. Initially, the Braille dot was convex and compressed at 55 °C, then the dot became flat and cooled to 25 °C. After unloading and reheating, the convex shape was recovered (Figure 8e). Before T attained 45 °C, the shape of a single Braille dot remained unrecovered in the "OFF" state, demonstrating the feasibility of the SRBDD-PL-MRE. The recovery process of a single Braille dot further showed the good resilience of the PL-MRE (Movie S1, Supporting Information). Owing to the in situ sensing property of the PL-MRE, the Braille device possessed feedback capability. Once the Braille dots were touched, the PL-MRE around the touched dot was compressed, which led to resistance variation. The electrical sensing signal of these areas was then collected through the copper tapes, while no current passed through the Braille dots. Therefore, the SRBDD-PL-MRE was not hazardous for blind people, and the position of the touched Braille dots could be determined, which promoted the interaction between people and devices. By pressing the same area several times, the σ quickly increased and returned to its original state as the finger touched and released (Figure 8f). When compressing the Braille dots on the boundary, the compressed area (dark green squares) around the touched Braille dots (blue circles) was accurately displayed by the SRBDD-PL-MRE (Figure 8g). Thus, the touched Braille dots could be clearly distinguished by the device owing to the in situ sensing capability. To further prove the feasibility of SRBDD-PL-MRE, an NIR laser was employed to heat different Braille dots on the surface. The device was heated and compressed to retain the "OFF" state initially. The Braille letters "U," "S," "T," and "C" were then displayed with different programs using a laser (Figure 8h). From the enlarged figure, a Braille text consisting of convex and flat Braille dots could be found with stable tactile sensation, which successfully achieved the functions of a touchable, conductive, and refreshable SRBDD-PL-MRE.

3. Conclusion

In summary, a magnetoresistive composite (PL-MRE) with multiple sensitivity and triple-shape memory effects was fabricated. Different temperatures allowed the shape fixation and recovery of the PL-MRE owing to the existence of two temperature-controlling components (PCL and HLM). The introduction of CIPs resulted in a PL-MRE with a special magneto-induced capability. Thus, the PL-MRE composite could effectively respond to an external compressive strain and magnetic flux density of 135.9 and 3.10 T^{-1}, respectively, with sensitivity. Finally, a novel SRBDD based on the PL-MRE (SRBDD-PL-MRE) was developed. No high-voltage power supply was required to actuate this device, and no current crossed the touched area, making it safe for the human body. Each Braille dot could be triggered by an NIR laser to display Braille texts consisting of different Braille letters. The presented SRBDD-PL-MRE realized the integration of easy fabrication, safety, and stable display capability, allowing it to serve as a convenient Braille e-book and promising large-scale Braille devices in the future.

4. Experimental Section

Materials: First, PCL pellets (Zhanyang Polymer Material Co., Ltd. China) were melted at 80 °C, turning them into a transparent gel. This was completely blended in PDMS (Sylard 184, Dow Corning) precursor with weight ratios of 10 to 70 wt%. After the mixture was cooled, the PDMS curing agent was added and the mixture was cured for 25 min at 80 °C, and the PDMS-PCL was fabricated. After HLM (44.7 wt% Bi, 22.6 wt% Pb, 19.1 wt% In, 8.3 wt% Sn, and 5.3 wt% Cd, Yongcheng Metal Material Co., Ltd. China) and CIPs (type CN, BASF) was added to the PDMS-PCL precursor and fully stirred at 80 °C, the PDMS-PCL-LM and PL-MRE precursors were obtained. Here, the volume fraction of HLM in PDMS-PCL-LM ranged from 10 to 65 vol%, and the volume fraction of CIPs in PL-MRE ranged from 7 to 28 vol%. These mixtures were fully stirred for several hours until all the PCL, HLM droplets, and CIPs were homogenously dispersed in the PDMS matrix. Finally, the PDMS curing agent was added to the cooled precursor, and the mixture was further cured for 25 min at 80 °C, and the PDMS-PCL-LM and PL-MRE were fabricated. During the curing process, a magnetic power system (IGLF-150, Beijing Saidi New Electromechanical Technology Co., China) was employed to generate a 1 T magnetic field for the pre-structuring of PL-MRE. The as-made PDMS-PCL, PDMS-PCL-LM, and PL-MRE samples are shown in Figure 1a. Here, the samples were defined as X wt%–Y vol%, where X is the weight ratio of PCL in the PDMS-PCL precursor, and Y is the volume fraction of HLM and CIPs in the whole sample.

Characterization: The morphologies of PDMS-PCL, PDMS-PCL-LM, and PL-MRE were characterized using scanning electron microscopy (SEM, Gemini 500, Carl Zeiss Jena Germany) and the digital and thermal images were captured using a digital camera (D1700, Nikon) and thermal camera (ImageIR 8300, InfraTec Germany). HyMDC (Hysteresis Measurement of Soft and Hard Magnetic Materials, Leuven, Belgium) was used to measure the saturated magnetization of PL-MRE. A Physica MCR 302 rheometer (Anton Paar Co., Austria) and a dynamic mechanical analyzer (DMA, ElectroForce 3200, TA instruments, Minnesota 55344 USA) were used to test the shear rheological, tensile, compression, and magneto-induced performance. During the compression and magnetic sensing tests, the PL-MRE samples were sandwiched using a copper foil. Signal wires were used to connect the PL-MRE to the Modulab material test system (Solartron Analytical, AMETEK Advanced Measurement Technology, Inc., UK) to evaluate the response performance. A 3D printer (Flashforge, Ltd., China) was employed to fabricate the molds, and NIR laser (808 nm, Fuzhe Technology Co., Ltd) was employed to trigger the SRBDD-PL-MRE.

Supporting Information

Supporting Information is available from the Wiley Online Library or from the author.

Acknowledgements

Financial supports from the National Natural Science Foundation of China (Grant Nos. 11822209, 12072338, 11972343, 12132016), the Anhui's Key R&D Program of China (202104a05020009), the Fundamental Research Funds for the Central Universities (WK2480000007, WK2480000009), Joint Fund of USTC-National Synchrotron Radiation Laboratory (KY2090000055), and Strategic Priority Research Program of the Chinese Academy of Sciences (Grant No. XDB22040502) are gratefully acknowledged.

Conflict of Interest

The authors declare no conflict of interest.

Data Availability Statement

The data that support the findings of this study are available from the corresponding author upon reasonable request.

Keywords

Braille devices, high-temperature liquid metal, magnetorheological elastomer, multifunctional composite, triple shape memory effect

Received: June 27, 2021
Revised: August 14, 2021

---

[1] A. Sterr, M. M. Muller, T. Elbert, B. Rockstroh, C. Pantev, E. Taub, *Nature* **1998**, *391*, 134.
[2] M. J. Tobin, *Nature* **1971**, *232*, 70.
[3] R. W. Heinrichs, J. A. Moorhouse, *N. Engl. J. Med.* **1969**, *280*, 72.
[4] S. Millar, *Br. J. Med. Psychol.* **1975**, *66*, 193.
[5] W. H. Dobelle, M. G. Mladejovsky, J. R. Evans, T. S. Roberts, J. P. Girvin, *Nature* **1976**, *259*, 111.
[6] A. C. Grant, M. C. Thiagarajah, K. Sathian, *Percept. Psychophys.* **2000**, *62*, 301.
[7] G. H. Feng, S. Y. Hou, *Sens. Actuators, A* **2018**, *275*, 137.
[8] K. Fukuda, T. Sekitani, U. Zschieschang, H. Klauk, K. Kuribara, T. Yokota, T. Sugino, K. Asaka, M. Ikeda, H. Kuwabara, T. Yamamoto, K. Takimiya, T. Fukushima, T. Aida, M. Takamiya, T. Sakurai, T. Someya, *Adv. Funct. Mater.* **2011**, *21*, 4019.
[9] Y. Ming, Y. Yang, R. P. Fu, C. Lu, L. Zhao, Y. M. Hu, C. Li, Y. X. Wu, H. Liu, W. Chen, *Adv. Mater. Technol.* **2018**, *3*, 1800257.
[10] D. Leonardis, C. Loconsole, A. Frisoli, *Meccanica* **2020**, *55*, 1639.
[11] Y. Zhang, S. F. Yang, J. R. G. Evans, *J. Am. Ceram. Soc.* **2004**, *87*, 2301.
[12] J. Y. Chung, A. Vaziri, L. Mahadevan, *Proc. Natl. Acad. Sci. USA* **2018**, *115*, 7509.
[13] Y. Haga, W. Makishi, K. Iwami, K. Totsu, K. Nakamura, M. Esashi, *Sens. Actuators, A* **2005**, *119*, 316.
[14] P. Chakraborti, H. A. K. Toprakci, P. Yang, N. Di Spigna, P. Franzon, T. Ghosh, *Sens. Actuators, A* **2012**, *179*, 151.
[15] X. C. Qu, X. Ma, B. J. Shi, H. Li, L. Zheng, C. Wang, Z. Liu, Y. B. Fan, X. Y. Chen, Z. Li, Z. L. Wang, *Adv. Funct. Mater.* **2021**, *31*, 2006612.
[16] Y. K. Bai, J. W. Zhang, D. D. Wen, B. Yuan, P. W. Gong, J. M. Liu, X. Chen, *J. Mater. Chem. A* **2019**, *7*, 20723.
[17] S. S. Wu, W. Li, Y. Q. Sun, X. L. Pang, X. J. Zhang, J. L. Zhuang, H. R. Zhang, C. F. Hu, B. F. Lei, Y. L. Liu, *J. Mater. Chem. C* **2020**, *8*, 8935.
[18] A. Lendlein, H. Y. Jiang, O. Junger, R. Langer, *Nature* **2005**, *434*, 879.
[19] W. S. Miao, W. K. Zou, B. J. Jin, C. J. Ni, N. Zheng, Q. Zhao, T. Xie, *Nat. Commun.* **2020**, *11*, 4257.
[20] Q. Zhao, H. J. Qi, T. Xie, *Prog. Polym. Sci.* **2015**, *49–50*, 79.
[21] A. Lendlein, O. E. C. Gould, *Nat. Rev. Mater.* **2019**, *4*, 116.
[22] J. K. Yuan, W. Neri, C. Zakri, P. Merzeau, K. Kratz, A. Lendlein, P. Poulin, *Science* **2019**, *365*, 155.
[23] S. Qi, J. Fu, Y. P. Xie, Y. P. Li, R. Y. Gan, M. Yu, *Compos. Sci. Technol.* **2019**, *183*, 107817.
[24] M. A. Darabi, A. Khosrozadeh, Y. Wang, N. Ashammakhi, H. Alem, A. Erdem, Q. Chang, K. G. Xu, Y. Q. Liu, G. X. Luo, A. Khademhosseini, M. Xing, *Adv. Sci.* **2020**, *7*, 1902740.
[25] S. Park, N. Baugh, H. K. Shah, D. P. Parekh, I. D. Joshipura, M. D. Dickey, *Adv. Sci.* **2019**, *6*, 1901579.
[26] J. A. C. Liu, B. A. Evans, J. B. Tracy, *Adv. Mater. Technol.* **2020**, *5*, 2000147.
[27] E. J. Markvicka, M. D. Bartlett, X. N. Huang, C. Majidi, *Nat. Mater.* **2018**, *17*, 618.
[28] M. J. Ford, D. K. Patel, C. F. Pan, S. Bergbreiter, C. Majidi, *Adv. Mater.* **2020**, *32*, 2002929.
[29] M. D. Bartlett, N. Kazem, M. J. Powell-Palm, X. N. Huang, W. H. Sun, J. A. Malen, C. Majidi, *Proc. Natl. Acad. Sci. USA* **2017**, *114*, 2143.
[30] A. F. Silva, H. Paisana, T. Fernandes, J. Gois, A. Serra, J. F. J. Coelho, A. T. de Almeida, C. Majidi, M. Tavakoli, *Adv. Mater. Technol.* **2020**, *5*, 2000343.
[31] G. L. Yun, S. Y. Tang, Q. B. Zhao, Y. X. Zhang, H. D. Lu, D. Yuan, S. S. Sun, L. Deng, M. D. Dickey, W. H. Li, *Matter* **2020**, *3*, 824.
[32] Y. M. Xin, Y. Lou, H. Z. Liu, D. F. Wu, J. Y. Zhang, *Adv. Mater. Technol.* **2021**, *6*, 2000852.
[33] M. G. Saborio, S. X. Cai, J. B. Tang, M. B. Ghasemian, M. Mayyas, J. L. Han, M. J. Christoe, S. H. Peng, P. Koshy, D. Esrafilzadeh, R. Jalili, C. H. Wang, K. Kalantar-Zadeh, *Small* **2020**, *16*, 1903753.
[34] C. F. Pan, D. Y. Liu, M. J. Ford, C. Majidi, *Adv. Mater. Technol.* **2020**, *5*, 2000754.
[35] T. V. Neumann, M. D. Dickey, *Adv. Mater. Technol.* **2020**, *5*, 2000070.
[36] G. L. Yun, S. Y. Tang, S. S. Sun, D. Yuan, Q. B. Zhao, L. Deng, S. Yan, H. P. Du, M. D. Dickey, W. H. Li, *Nat. Commun.* **2019**, *10*, 1300.
[37] Y. Lou, H. Z. Liu, J. Y. Zhang, *Chem. Eng. J.* **2020**, *399*, 125732.
[38] A. Fassler, C. Majidi, *Adv. Mater.* **2015**, *27*, 1928.
[39] Y. M. Xin, S. L. Zhang, Y. Lou, J. Xu, J. Y. Zhang, *Adv. Mater. Technol.* **2020**, *5*, 2000018.
[40] S. Rich, S. H. Jang, Y. L. Park, C. Majidi, *Adv. Mater. Technol.* **2017**, *2*, 1700179.
[41] L. F. Zhu, Y. Z. Chen, W. H. Shang, S. Handschuh-Wang, X. H. Zhou, T. S. Gan, Q. X. Wu, Y. Z. Liu, X. C. Zhou, *J. Mater. Chem. C* **2019**, *7*, 10166.
[42] X. Y. Wang, J. Y. Lan, P. P. Wu, J. Y. Zhang, *Polymer* **2021**, *212*, 123174.
[43] W. Q. Zhang, J. Z. Chen, X. Li, Y. Lu, *Small* **2020**, *16*, 2004190.
[44] S. Qi, H. Y. Guo, J. Fu, Y. P. Xie, M. Zhu, M. Yu, *Compos. Sci. Technol.* **2020**, *188*, 107973.
[45] Q. J. Ze, X. Kuang, S. Wu, J. Wong, S. M. Montgomery, R. D. Zhang, J. M. Kovitz, F. Y. Yang, H. J. Qi, R. K. Zhao, *Adv. Mater.* **2020**, *32*, 1906657.

[46] Y. Kim, H. Yuk, R. K. Zhao, S. A. Chester, X. H. Zhao, *Nature* **2018**, *558*, 274.
[47] Y. Alapan, A. C. Karacakol, S. N. Guzelhan, I. Isik, M. Sitti, *Sci. Adv.* **2020**, *6*, eabc6414.
[48] W. Q. Hu, G. Z. Lum, M. Mastrangeli, M. Sitti, *Nature* **2018**, *554*, 81.
[49] Z. J. Qi, M. X. Zhou, Y. Li, Z. Q. Xia, W. X. Huo, X. Huang, *Adv. Mater. Technol.* **2021**, *6*, 2001124.
[50] R. Ahamed, S.-B. Choi, M. M. Ferdaus, *J. Intell. Mater. Syst. Struct.* **2018**, *29*, 2051.
[51] Y. Li, J. Li, *Smart Mater. Struct.* **2017**, *26*, 045001.
[52] G. Liao, Y. Xu, F. Wei, R. Ge, Q. Wan, *J. Intell. Mater. Syst. Struct.* **2017**, *28*, 728.
[53] S. S. Sun, T. Yildirim, J. Wu, J. Yang, H. Du, S. W. Zhang, W. H. Li, *Smart Mater. Struct.* **2017**, *26*, 095039.
[54] S. Liu, S. Wang, S. H. Xuan, S. S. Zhang, X. W. Fan, H. Jiang, P. G. Song, X. L. Gong, *ACS Appl. Mater. Interfaces* **2020**, *12*, 15675.
[55] T. Hu, S. H. Xuan, L. Ding, X. L. Gong, *Sens. Actuators, B* **2020**, *314*, 128095.
[56] L. Ding, S. H. Xuan, L. Pei, S. Wang, T. Hu, S. S. Zhang, X. L. Gong, *ACS Appl. Mater. Interfaces* **2018**, *10*, 30774.
[57] T. Hu, S. H. Xuan, L. Ding, X. L. Gong, *Mater. Des.* **2018**, *156*, 528.
[58] L. Ding, L. Pei, S. H. Xuan, X. W. Fan, X. F. Cao, Y. Wang, X. L. Gong, *Adv. Electron. Mater.* **2020**, *6*, 1900653.
[59] X. L. Gong, Y. C. Fan, S. H. Xuan, Y. G. Xu, C. Peng, *Ind. Eng. Chem. Res.* **2012**, *51*, 6395.